

OHQ: On-chip Hardware-aware Quantization

Wei Huang ^{*1} Haotong Qin ^{*23} Yangdong Liu ³ Jingzhuo Liang ³ Yunlun Zhang ² Ying Li ^{✉3} Xianglong Liu ³

Abstract

Quantization emerges as one of the most promising approaches for deploying advanced deep models on resource-constrained hardware. Mixed-precision quantization leverages multiple bit-width architectures to unleash the accuracy and efficiency potential of quantized models. However, existing mixed-precision quantization suffers exhaustive search space that causes immense computational overhead. The quantization process thus relies on separate high-performance devices rather than locally, which also leads to a significant gap between the considered hardware metrics and the real deployment. In this paper, we propose an **On-chip Hardware-aware Quantization** (OHQ) framework that performs hardware-aware mixed-precision quantization without accessing online devices. First, we construct the *On-chip Quantization Awareness* (OQA) pipeline, enabling perceive the actual efficiency metrics of the quantization operator on the hardware. Second, we propose *Mask-guided Quantization Estimation* (MQE) technique to efficiently estimate the accuracy metrics of operators under the constraints of on-chip-level computing power. By synthesizing network and hardware insights through linear programming, we obtain optimized bit-width configurations. Notably, the quantization process occurs on-chip entirely without any additional computing devices and data access. We demonstrate accelerated inference after quantization for various architectures and compression ratios, achieving 70% and 73% accuracy for ResNet-18 and MobileNetV3, respectively. OHQ improves latency by 15~30% compared to INT8 on deployment.

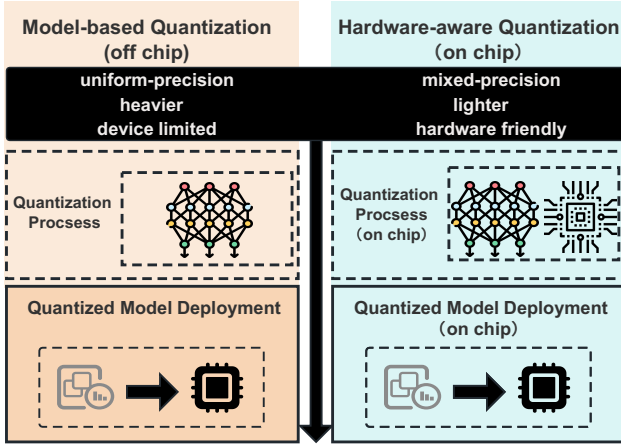


Figure 1. Off-chip vs. on-chip Quantization. The left shows the traditional off-chip quantization framework involving quantization analysis and deployment steps. The right part is our OHQ framework, which is fully integrated on-chip.

1. Introduction

Recently, the deep neural network (DNN) has achieved significant development and shown its great potential in various fields, such as computer vision, and natural language processing. The advancement of DNN can be mainly attributed to the rapid expansion of parameters and the increasing depth of the model. Although over-parameterization has enhanced the performance of DNNs, it has simultaneously posed a serious challenge when deploying real-time inference in resource-constrained edge devices. Edge chips impose stricter constraints on memory footprint, energy consumption, and latency(Horowitz, 2014). An intuitive solution to mitigate this issue is quantizing the full-precision 32-bit weights and activations of DNNs to low-bit integers or binaries (Gray & Neuhoff, 1998; Han et al., 2015; Lin et al., 2017; Zhu et al., 2016). The basic quantization involves uniformly compressing all layers of a DNN to a consistent bit-width (Choi et al., 2018; Krishnamoorthi, 2018), which overlooks the computational redundancies inherent in different operator layers within the network and subsequently neglects the varying impact on overall performance. To address this limitation, it becomes imperative to adopt variable bit-widths for distinct layers, a concept known as mixed-precision quantization (Cai et al., 2020; Ma et al., 2023; Wu et al., 2018; Yao et al., 2021). The mixed-precision quantization considers the operators with different bit widths in search space optimization, which significantly

^{*}Equal contribution ¹The University of Hong Kong ²ETH Zürich ³Beihang University. Correspondence to: [✉]Ying Li <lyinging@buaa.edu.cn>.

pushes the accuracy and efficiency limits of quantized NNs. However, it also causes significant computation overhead in the quantization process. In a L -layers DNN, the S number of bit-width candidates results in a computation with $O(S^L)$ complexity. This exemplifies an exponential increase in computational demand for mixed-precision strategies, especially pronounced in deeper architectures.

These facts introduce strong motivation to construct an on-chip mixed-precision quantization framework that harmoniously integrates the quantization algorithm with real hardware. The challenges in constructing this quantization framework stem from two main aspects: (1) Hardware awareness: Since the need to consider the accuracy and speed of quantized models based on their deployed hardware, this framework should on-chip perceive various metrics of operators on real hardware, including but not limited to latency and memory usage. This framework should achieve hardware awareness for the deployed devices. (2) Lightweight process: Given the necessity to thoroughly consider efficiency-oriented hardware metrics, the expanded search space requires an efficient yet resource-lightweight algorithm for on-chip quantization processes. This ensures that the quantization process does not rely on external computational and data resources. Despite the presence of certain hardware awareness and mixed-precision quantization techniques that emerged earlier (Cai et al., 2020; Dong et al., 2020; Ma et al., 2023; Wang et al., 2019; Yang & Jin, 2021; Yao et al., 2021), they still exhibit some significant issues that cannot be overlooked. These issues include the computationally expensive nature of the process and reliance on inaccurately estimated hardware metrics, among others. These factors hinder their progression toward becoming the ideal on-chip quantization methods.

In this work, we propose an On-chip Hardware-aware Quantization (OHQ) framework (see Fig. 1) to overcome the above-mentioned issues. The proposed OHA mainly relies on two novel techniques: the *On-chip Quantization Awareness* (OQA) pipeline enables perceiving the actual efficiency metrics of the quantization operator on the hardware, which uses synthetic data as input to obtain the latency, memory usage, and power metrics on-chip. Second, we propose *Mask-guided Quantization Estimation* (MQE) technique to efficiently estimate the accuracy metrics of operators under the constraints of on-chip-level computing power, and then we can search for optimized bit-width configurations simplified as linear programming. Our comprehensive experiments show that OHQ outperforms existing mixed-precision quantization methods in accuracy and efficiency by a substantial margin. We also demonstrate the effectiveness of our OHA on various networks, such as ResNet-18/50 and MobileNetV2/V3, highlighting its versatility across architectures. We summarize our contributions as follows:

- We propose a mixed-precision quantization framework OHQ, which is a totally on-chip design from quantization computation to deployment. By employing edge computing chips as co-processors alongside on-chip central processing units (CPUs) for the quantization, compression, and inference computations of neural networks, we effectively eliminate the necessity for auxiliary computing devices.
- A hardware-aware method OQA that operates at the Intellectual Property (IP) core granularity is first proposed. This approach utilizes the chip’s clock cycle consumption per computational layer as a metric for hardware, while simultaneously considering the constraints imposed by the available computational power.
- We develop an enhanced and statistically robust sensitivity metric MQE for performing small-batch distilled data inference on edge devices, which support data-free sensitivity feedback and quantization.
- We additionally furnish comprehensive empirical findings for ResNet18/50 (He et al., 2016), MobileNetV2/V3 (Howard et al., 2019). These findings delineate both the state-of-the-art quantization outcomes achievable in real-world edge scenarios, and further illustrate that this mixed-precision strategy is applicable to both the Post-Training Quantization (PTQ) and Quantization-Aware Training (QAT) approach.

2. Related Work

2.1. Mixed-Precision Quantization

Quantization maps parameters \mathbf{x} to fixed-point ranges using the following equation:

$$\text{quantize}(\mathbf{x}) = \text{round}(\mathbf{x}/S) - \mathbf{z}, \quad (1)$$

where quantize denotes quantization function, S and \mathbf{z} denote the scaling factor and zero-point, respectively. Existing quantization approaches can be divided into quantization-aware training (QAT) and post-training quantization (PTQ). QAT quantizes the network throughout the training process with the original dataset, resulting in accurate quantization while markedly computation overhead (Choi et al., 2018; Wang et al., 2019; Yao et al., 2021). PTQ operates as an offline algorithm, it relies on a few real or synthetic samples to calibrate the quantization functions of weights and activations, thus just utilizing much less computation in the quantization process compared to QAT (Cai et al., 2020; Li et al., 2021; Nagel et al., 2019).

For utilizing the accuracy and efficiency potential of the quantized model, mixed-precision quantization emerges as a promising way, which enables accuracy-sensitive layers

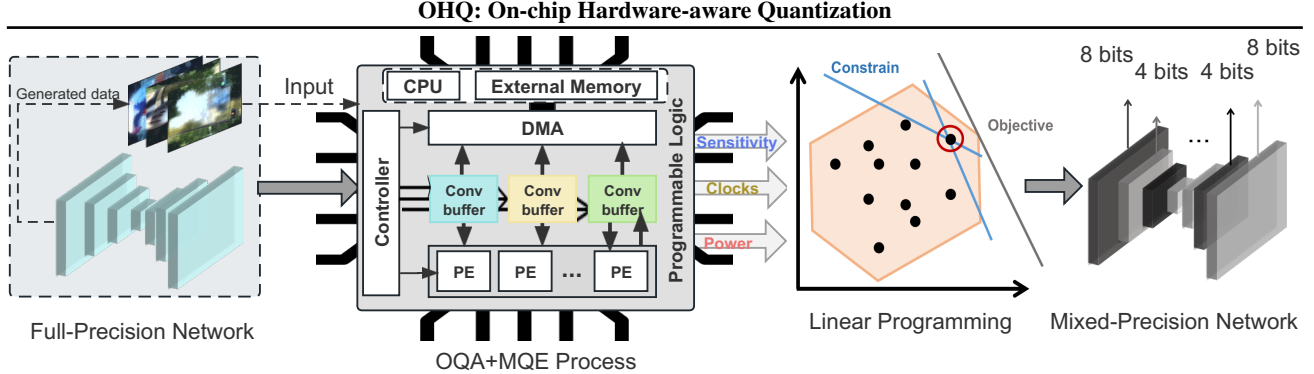


Figure 2. The overview of OHQ framework. This proposed OHQ obtains chip-level sensing parameters and layer-wise differences through a physical deployment (OQA and MQE are respectively described in detail in Fig. 3 and Fig. 4).

to retain high precision (i.e., more bit-widths) while others maintain low precision (Dong et al., 2023; 2020; Ma et al., 2023; Shen et al., 2020; Wang et al., 2019; Zhou et al., 2018). Nevertheless, a major challenge associated with this strategy lies in identifying the optimized mixed-precision configuration since the search space exhibits an exponential relationship with the number of layers, particularly in resource-limited scenarios. Thus, various mixed-precision quantization methods are proposed to improve this. Dong et al. use a second-order Hessian matrix as an accuracy sensitivity metric for each layer (Dong et al., 2019) and also apply the mean of the eigenvalues of the Hessian to mitigate computational overhead (Dong et al., 2020). (Qin et al., 2023) and (Cai et al., 2020) propose data-free methods to get rid of the reliance on the data resource on edge. However, it is hard for existing methods to achieve on-chip mixed-precision quantization accurately and efficiently.

2.2. Hardware-Aware Quantization

The accuracy sensitivity of quantized layers can frequently be described as the influence of quantization on the model accuracy. However, the computational expenditure of network operators on physical hardware should also serve as a constraint for bit-width configuration, incorporating aspects such as latency and energy consumption. The heavily consuming layers should be quantized to low precision, while the light-consuming ones should be retained to high precision. Wang et al. (Wang et al., 2019) investigated the allocation of bit-width across various hardware architectures using a reinforcement learning model. This approach, described as a black-box strategy, relies on the perception of hardware characteristics. However, this exploration approach is computationally complex and difficult to realize offline quantization. Yao et al. (Yao et al., 2021) identified the computation time of each network layer as a constraint for allocating bit-widths, implementing this approach by deploying the quantized network on a Graphics Processing Unit (GPU). However, the roughly obtained computation time is affected by software, operating system (OS), and

network transmission, and cannot reflect the on-chip computational efficiency accurately.

We select FPGA to implement and evaluate our framework since it serves as a flexible and reliable hardware platform for DNN deployment(Guo et al., 2017; Shawhna et al., 2018) and validating Application-Specific Integrated Circuit (ASIC) designs through accurate flow verification methodologies(Boutros et al., 2018; Farooq & Mehrez, 2021; Hutton et al., 2006; Markovic et al., 2007). We proposed a fine-grained hardware awareness by clock cycles and energy, which can achieve a more accurate representation of hardware computation consumption at the IP core level. This methodology enables a closer examination of the chip's underlying layer, thereby facilitating a realistic construction of the computational connection between DNNs and chips.

3. Methodology

In this section, we present our On-Chip Hardware-Aware Quantization (OHQ) framework (see Fig. 2), including the On-Chip Quantization Awareness (OQA) pipeline and Mask-Guided Quantization Estimation (MQE) technique.

3.1. On-Chip Quantization Awareness

3.1.1. GENERATED SYNTHETIC DATA

The statistics of the BN layer in the full-precision model, namely the mean standard deviation, correspond to the real dataset in the training process. Consequently, the majority of data-free quantization schemes(Cai et al., 2020; Haroush et al., 2020; He et al., 2021; Nagel et al., 2019; Qin et al., 2023) employ BN statistical losses to capitalize on the information present in the BN layer. The subsequent optimization objectives facilitate the congruence of synthetic data distribution x^d with the BN statistics:

$$\min_{x^d} \mathcal{L}_{\text{distill}} = \sum_{i=1}^L \|\tilde{u}_i^d - u_i\|_2^2 + \|\tilde{\sigma}_i^d - \sigma_i\|_2^2, \quad (2)$$

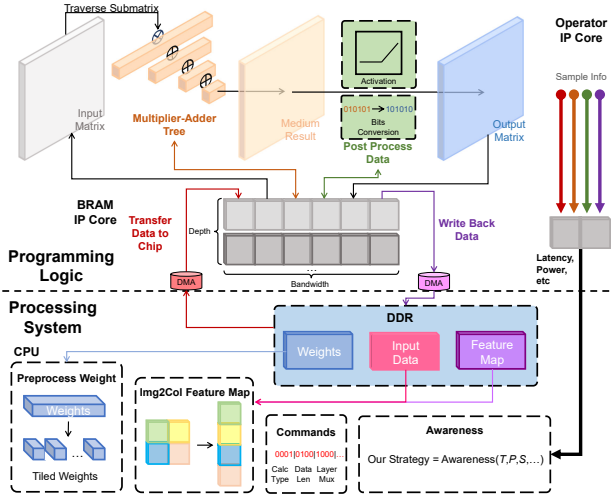


Figure 3. The workflow of OQA. (Top) The PL part samples time, power, and other information of four main steps for awareness while computing, which use BRAM to optimize matrix multiplication and data transfer. (Bottom) The PS part controls the whole situation, including accessing data, organizing the network, and instructing IP cores.

where u_i and σ_i are the mean and standard deviation parameters of the pre-trained model’s BN layer. \tilde{u}_i^d and $\tilde{\sigma}_i^d$ represent the mean and standard, respectively, of the feature matrix generated by x^d at the i -th of the BN layer. Eq. 2 is to minimize the statistical loss $\mathcal{L}_{distill}$ in each BN layer of the original model, and ultimately to generate synthetic data that matches the input data distribution. Our distilled data is inputted directly into the FPGA, which ascertained the following hardware awareness and MQE technique. This approach aims to bolster the operational efficiency of the proposed framework.

3.1.2. HARDWARE AWARENESS

While previous study(Yao et al., 2021) has recommended the use of cloud GPU running time as a hardware-aware constraint, this coarse-grained metric is influenced by the OS, and application layers’ latency and does not provide a comprehensive reflection of the DNN’s performance on the physical chip(Nurvitadhi et al., 2016; Yang et al., 2012). To comprehend the finer-grained hardware constraints, we observed the IP core level network operations on FPGAs and named it OQA.

To enable network deployment on FPGAs, we employ a two-step process: first, quantizing and compiling the model post-acquisition, and then translating the layers into their respective arithmetic module implementations. This is complemented by the introduction of a central controller.

- 1) Img2Col: Converts layer data from discontinuous storage to continuous storage, streamlining transmission and computation.

- 2) Multiplication and addition tree: Utilizes parallel stacking and cascading multiplication and addition mechanisms to enable simultaneous pointwise multiplication computation across vast amounts of data.
- 3) Sub-matrix slicing transmission and computation: Divides a large matrix into multiple tiles for transmission to the chip, performing computation and splicing on these tiles to alleviate FPGA resource pressure.
- 4) BRAM large bandwidth fill: The primary storage mechanism employed in on-chip Block Random Access Memory (BRAM), which is divided into rows to facilitate the reading and writing of large bit-width data simultaneously, ensuring computation and access remain logically and physically coherent.

The above methods enable efficient parallel computation of networks, and a reasonable quantitative deployment scheme is formulated with full consideration of the resource and power constraints of hardware.

Our proposed clock-aware approach, predicated on the interaction between the IP core and the BRAM, is illustrated in Fig. 3. During runtime, the IP core on the Programmable Logic (PL) side—which is responsible for four steps including computation of weight and feature map, data transfer, data write-back, and data post-process—automatically collects the number of running clock cycles and stores them in the target BRAM. Then, the FPGA-compatible transmission mechanism relays the collected clock cycles to the Processing System (PS) side. This can be denoted as $[c_1, \dots, c_i, \dots, c_L]$, c_i represents the total number of clock cycles in the i -th layer. Concurrently, the power consumption of the IP core during computation is diminished as $[e_1, \dots, e_i, \dots, e_L]$.

Note that OQA is the first pipeline to propose fine-grained sensing at the chip IP core level. By obtaining the clock information of each of the four calculation steps from the PL, we get the exact part of the operation of each layer on-chip to optimize MQE.

3.2. Mask-Guided Quantization Estimation

3.2.1. LAYERWISE SENSITIVITY ON HARDWARE

DNN models comprise L layers of computational units, which can be represented as $[U_1, U_2, \dots, U_L]$, wherein U_i denotes the i -th layer computational unit. The learnable parameters (e.g., weights) are denoted as $[\theta_1, \theta_2, \dots, \theta_L]$, where $\theta \in \mathcal{R}^n$ is float32 type data in full-precision models. Layer-wise sensitivity typically corresponds to the impact of distinct layers within a network on the output results. As previously discussed, sensitivity measurement using the Hessian matrix can be computationally intensive. An alternative approach involves quantizing U_i to 4/8 bits while

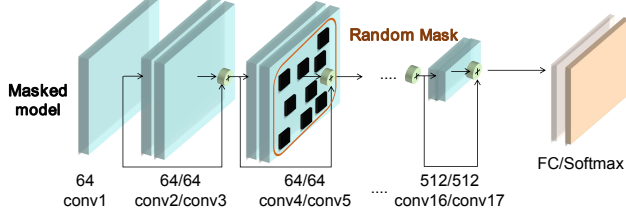


Figure 4. Illustration of MQE for ResNet18. Specifically, we feed synthesized data into on-chip models. The figure shows the model with the 5-th layer specifically masked out.

maintaining full precision for the remaining layers:

$$\theta_i^q = \text{quantize}(\theta_i), \quad (3)$$

$$\begin{cases} \mathcal{M} = F(U_1(\theta_1); \dots; U_i(\theta_i); \dots; U_L(\theta_L)), \\ \mathcal{M}_i^q = F(U_1(\theta_1); \dots; U_i^q(\theta_i^q); \dots; U_L(\theta_L)), \end{cases} \quad (4)$$

where θ_i^q is the quantized parameters in i -th layer and the bit width, q is the selected bit-widths, F denotes the general function of NN model, \mathcal{M} represents the full-precision model, \mathcal{M}_i^q denotes the quantized model with quantized layer U_i^q . Then, the performance difference is calculated by the following equation:

$$\omega_i = \frac{1}{N} \sum_{j=1}^N f(\mathcal{M}(x_j), \mathcal{M}_i^q(x_j)), \quad (5)$$

where ω_i indicated the sensitivity value of the i -th layer, N is the batch-size of distilled data used for inference, $f(\cdot, \cdot)$ denotes the sensitivity calculation function that compares the output of \mathcal{M} and \mathcal{M}_i^q , and x is the input data.

Nonetheless, this method necessitates the quantization L times, resulting in considerable computational overhead for so many quantizations processed. Consequently, this sensitivity calculation presents challenges for on-chip deployment. Therefore, we introduce a masked-guided technique (MQE) displayed in Fig. 4, which is more efficient and suitable for on-chip implementation:

$$\tilde{\theta}_i^q = g(\alpha, \theta_i^q), \quad (6)$$

$$\begin{cases} \mathcal{M}^q = F(U_1^q(\theta_1^q); \dots; U_i^q(\theta_i^q); \dots; U_L^q(\theta_L^q)), \\ \tilde{\mathcal{M}}_i^q = F(U_1^q(\theta_1^q); \dots; \tilde{U}_i^q(\tilde{\theta}_i^q); \dots; U_L^q(\theta_L^q)), \end{cases} \quad (7)$$

where $g(\cdot, \cdot)$ denotes the masking operator, α is the mask ratio, and $\tilde{\theta}_i^q$ is the mask result of θ_i^q . To facilitate the on-chip test of FPGA, the parameters must first undergo integer bit-wise quantization (in this case, $q = 8$). Subsequently, the parameters of the target layer are randomly masked by setting them to 0, and the α is selected as 0.5 to map the loss of information loss from 8 bits to 4 bits. In MQE, only 1 time quantization of the DNN is necessary. Despite

the requirement for L masking operations, their computational consumption is considerably less compared to that of quantization computation. Then, we use the KL divergence:

$$\begin{aligned} D_{kl}(p \parallel q) &= -\sum_x p(x) \log q(x) - \sum_x -p(x) \log p(x), \\ &= \sum_x p(x) \log \frac{p(x)}{q(x)}, \end{aligned} \quad (8)$$

where $p(x)$ and $q(x)$ denote two probability distributions of the original model and masked model. KL divergence can determine the disparity in output distribution between the original and masked models, thereby effectively measuring the information entropy between the matrices. Then, we update Eq. 5 to get our sensitivity:

$$\omega_i = \frac{1}{N} \sum_{j=1}^N D_{kl}(\mathcal{M}^q, \tilde{\mathcal{M}}_i^q), \quad (9)$$

Our proposed MQE is obtained by inference on edge devices, which better reflects the layer-wise perception in NN in real hardware operation scenarios than simulation experiments on servers and GPUs. Consequently, the masking operations are negligible and can be swiftly executed by the CPU embedded within the edge device.

3.2.2. MIXED-PRECISION QUANTIZATION

Our findings reveal that the relationship between hardware consumption and model parameters is not entirely linear, demonstrating variability as depicted in Fig. 5. This observation validates the efficacy of our proposed OHQ framework in precisely assessing the performance of both the network and the hardware, underscoring the critical role of on-chip hardware awareness in the quantization process. Motivated by these insights, we aim to strike an optimal balance between model performance and hardware computational efficiency. Towards this end, we have formulated a quantitative constraint function that amalgamates On-chip OQA and MQE:

$$1 = \beta + \gamma, \quad (10)$$

$$\Omega_i = \beta \hat{\omega}_i - \frac{\gamma}{2} (\hat{c}_i + \hat{e}_i), \quad (11)$$

where β and γ are two hyper-parameters used to control the proportion of the sensitivity and hardware resources. To consider this hardware awareness fairly, we set β and γ to 0.5 in the subsequent experiments. The hyper-parameters can be manually modified to satisfy the personalized deployment for the precision and hardware compression rate. $\hat{\omega}_i$, \hat{c}_i and \hat{e}_i are scaled values from ω_i , c_i and e_i , which ensures that the different initial awareness value is in same the range

OHQ: On-chip Hardware-aware Quantization

Arch	Method	Int-Only	Uniform	W/A	Data	Size (Mb)	Latency(ms)	Top-1 (%)
ResNet18	Baseline	✗	-	32/32	1.2E6	44.6	39.6*	73.21
	Min&Max	✗	✓	8/8	1.2E6	11.1	78.3	71.38
	OHQ (ours)	✓	✓	8/8	†32	11.1	78.3	71.52
	FracBits-PACT‡(Choi et al., 2018)	✗	✓	*/*	1024	5.8	68.6	69.70
	ZeroQ(Cai et al., 2020)	✓	✓	*/*	†32	5.8	67.9	21.20
	BRECQ(Li et al., 2021)	✓	✓	*/8	1024	5.8	67.6	69.32
	OMPQ(Ma et al., 2023)	✓	✓	*/4	64	5.5	70.2	69.38
	EMQ(Dong et al., 2023)	✓	✓	*/4	64	5.5	-	70.12
ResNet50	OHQ (ours)	✓	✓	*/*	†32	5.5	63.5	70.18
	Baseline	✗	-	32/32	1.2E6	97.8	80.2*	77.72
	Min&Max	✗	✓	8/8	1.2E6	24.5	182.6	77.70
	OHQ (ours)	✓	✓	8/8	†32	24.5	182.6	77.72
	PACT‡(Choi et al., 2018)	✗	✓	*/*	1024	19.2	151.2	75.3
	OCS(Zhao et al., 2019)	✓	✓	6/6	1.2E6	18.4	159.6	74.80
	FIOPTQ(Chauhan et al., 2023)	✓	✓	*/8	2048	12.2	-	75.44
	ZeroQ(Cai et al., 2020)	✓	✓	*/6	†32	18.3	160.3	77.43
MobileNetV2	OHQ (ours)	✓	✓	*/*	†32	17.8	147.8	77.55
	Baseline	✗	-	32/32	1.2E6	13.4	11.3*	73.03
	Min&Max	✗	✓	8/8	1.2E6	3.3	100.7	70.29
	OHQ (ours)	✓	✓	8/8	†32	3.3	100.7	73.00
	FIOPTQ(Chauhan et al., 2023)	✓	✓	*/16	2048	3.4	-	71.38
	FracBits-PACT‡(Choi et al., 2018)	✓	✓	*/*	†32	1.8	85.4	69.90
	BRECQ(Li et al., 2021)	✓	✓	*/8	1024	1.5	81.7	70.28
	EMQ(Dong et al., 2023)	✓	✓	*/8	64	1.5	-	70.75
MobileNetV3	OHQ (ours)	✓	✓	*/*	†32	1.5	67.1	71.46
	Baseline	✗	-	32/32	1.2E6	15.3	10.6*	74.32
	Min&Max	✗	✓	8/8	1.2E6	3.9	85.0	72.98
	OHQ (ours)	✓	✓	8/8	†32	3.9	85.0	74.29
	OHQ (ours)	✓	✓	*/*	†32	2.4	73.4	73.01

Table 1. Results of PTQ methods with ResNet18, ResNet50, MobileNetV2, and MobileNetV3. † indicates using distilled data in the quantization process. * means the latency results are tested on the CPU, others are deployed on FPGA (batch=1). - is the lack of hardware deployment latency testing, which may be due to that the method has not disclosed the code or the precision preservation method is not being supported on our selected hardware chip.

$[0, 1]$ and Ω_i is the optimal factor of the i -th layer. Ultimately, we maximize the sum of Ω_i in the network through an integer linear programming (ILP) model:

$$\text{Objective : } \max_{\{b_i\}_{i=1}^L} \sum_{i=1}^L (b_i \Omega_i), \quad (12)$$

$$\text{Constrain : } \sum_{i=1}^L M_i^{b_i} \leq \text{Model Size Limit},$$

$M_i^{b_i}$ denotes the parameters size of the i -th layer under b_i bit-width quantization. The compression ratio of the target model is flexible. Since the selectable bit widths are 4 and 8, the target size should be between the uniform 4-bit model and the uniform 8-bit model. It is worth noting that compared to the reinforcement learning method proposed by Wang et al.(Wang et al., 2019) and the Hessian evaluation proposed by Dong et al.(Dong et al., 2020), the ILP model

only takes about 1 second to obtain the optimal bit-width configuration result under the hardware-aware result input condition. This computation is very efficient and can be done on the embedded CPU of the edge platform.

4. Experiment

In this subsection, a comprehensive array of experiments is undertaken to empirically validate the performance of the OHQ. The preliminary step encompasses the delineation of the datasets employed and the specific models selected for the experimental evaluations. The ablation experiments compare the decomposition of OQA and MQE. Conclusively, an intricate comparison is executed, juxtaposing the performance metrics of disparate models as facilitated by the OHQ framework. The results of this comparative assessment conspicuously highlight the discernible merits inherent in our proposed approach, manifesting in superior

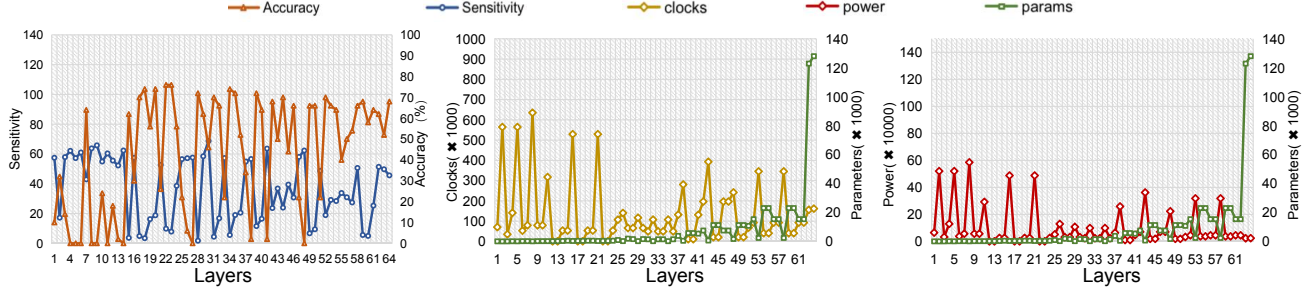


Figure 5. Comparison of MobileNetV3’s on-chip awareness characteristics and network parameters of each layer. The first image on the left demonstrates the relationship between the model accuracy (in orange) post-application of layer-wise masking and the sensitivity of that layer (in blue). The central image depicts the relationship between the on-chip computational clock (in yellow) for each layer and the number of parameters in the layer (in green). The image on the right presents the relationship between the on-chip power consumption (in red) for each layer and the number of layer parameters.

Arch	Method	W/A	Size (Mb)	Latency (ms)	Top-1 (%)
	PACT‡(Choi et al., 2018)	5/5	7.2	70.4	69.80
	HAWQ-v3(Yao et al., 2021)	*/*	7.3	72.9	70.01
ResNet18	OMPQ(Ma et al., 2023)	*/6	6.7	-	72.08
	EMQ(Dong et al., 2023)	*/6	6.7	74.2	72.28
	OHQ (ours)	*/*	6.9	68.3	71.87
	HAWQ-v3(Yao et al., 2021)	*/*	18.7	172.1	75.39
ResNet50	OMPQ(Ma et al., 2023)	*/5	18.7	185.4	76.28
	OHQ (ours)	*/*	16.5	135.9	76.64
	GZNQ(He et al., 2021)	6/6	2.5	81.7	71.10
MobileNetV2	HAQ(Wang et al., 2019)	*/*	1.8	75.5	71.47
	OHQ (ours)	*/*	1.7	70.1	72.56

Table 2. Results of QAT with ResNet18/50 and MobileNetV2. ‡ means not quantizing the first and last layers. - is the lack of hardware deployment latency testing, which may be due to the method not disclosing the code or the precision preservation method is not supported on our selected hardware chip.

compression rates, heightened operational performance, and enhanced quantization efficiency.

4.1. Implementation Details

We validate the experiments on ImageNet(Deng et al., 2009) dataset. The training data (1.5M) encompassing Imagenet was deliberately left unutilized in our study. Instead, only 32 distilled images are generated, specifically dedicated to the computational assessment of perceptual outcomes about OQA and MQE during the forward inference. Owing to the wide use of residual structures in DNNS, we chose the ResNet18 and ResNet50 networks. In addition, we also conduct experiments on MobileNetV2 and MobileNetV3.

Our experimentation and assessments are exclusively executed on an ECE-EMBD development board, housing components from the ZYNQ chip series. This development board amalgamates a dual-core ARM Cortex-A9 processor endowed with 512MB of DDR3 memory on the PS side. The memory subsystem is defined by the MT41K256M16TW model, boasting a 16-bit bit width. The

PL domain encompasses the XC7Z020-CLG400-1 chip, characterized by an assembly of 85K logic resources, and 140 BRAMs with a cumulative capacity of 4.9 Mb. Notably, the on-chip hardware sensing leverages a quantization strategy spanning from 4 bits to 8 bits, judiciously bounding matrix parallel operations to a maximum size of 128 data elements on a single facet. This prudent limitation is designed to preempt an overallocation of BRAM resources and thus preserve adherence to prescribed quotas.

4.2. Comparison Results

The important feature of the OHQ proposed in this paper is the on-chip, and in order to efficiently implement the model, we performed PTQ on ResNet18/50, MobileNetV2, and MobileNetV3. and compared it with previous methods (Cai et al., 2020; Li et al., 2021; Nagel et al., 2019; Park & Yoo, 2020; Yang & Jin, 2021; Zhao et al., 2019). Table 1 underscores OHQ as the optimal 8-bit quantization strategy across diverse networks. The optimal trade-off between precision and compression ratio in mixed-precision quantization is also shown. In the performance of ResNet18, an accuracy of 70.08% is attained, harmoniously juxtaposed with a compact footprint of 5.8 Mb and latency of 63.5 ms. Meanwhile, the ResNet50 model, compressed to a size of 17.8 Mb with a speed of 147.8 ms, exhibits an accuracy of 77.55%. The highest accuracy and lowest compression Rate and time were achieved in MobileNetV2 (71.64%, 1.7 Mb, 70.1 ms). Notably, the MobileNetV3 network attains an accuracy of 73.01% while preserving a remarkably small size of 2.4 Mb and latency of 73.4 ms.

We also combine QAT and OHQ due to the ability of the QAT method to improve quantization model accuracy through data retraining (shown in Table 2). In the ResNet18 network, we achieve, with only 6.9Mb of the model, 70.23% accuracy, which is ahead of HAWQ-v3 in terms of compression and performance. Notably, PACT does not quantize the input and output layers, and the activations are retained 23 bits from HAQ. For ResNet50, OHQ shows the best re-

Arch	Ratio	W/A	Vanilla		MQE		OQA		MQE + OQA	
			Size (Mb)	Top-1 (%)						
ResNet18	0.25	*/*	7.30	70.01	6.90	70.23	6.20	69.97	6.90	70.23
	0.50	*/*	7.90	70.50	8.30	71.31	7.30	70.05	7.70	71.25
	0.75	*/*	9.90	71.20	9.70	71.79	8.20	70.13	8.90	71.56
	0.80	*/*	10.70	71.91	10.00	72.53	10.00	71.12	10.00	72.53
ResNet50	0.25	*/*	16.00	74.89	15.47	75.00	14.21	72.64	15.10	74.72
	0.50	*/*	19.00	75.95	17.51	76.35	16.76	74.84	17.51	76.35
	0.75	*/*	21.30	77.38	20.50	77.44	19.20	75.01	19.82	77.19
	0.80	*/*	22.00	77.40	21.09	77.61	19.65	76.28	21.09	77.61
MobileNetV2	0.25	*/*	2.29	71.22	2.06	71.62	1.97	70.05	2.06	71.62
	0.50	*/*	2.51	71.46	2.54	71.75	2.13	71.33	2.43	71.70
	0.75	*/*	2.60	71.81	2.60	71.83	2.36	71.49	2.60	71.83
	0.80	*/*	2.75	72.08	2.70	72.79	2.61	71.81	2.70	72.79

Table 3. Ablation experiments of different optimization factors on ResNet18 and MobileNetV2. We select HAWQ-v3 as our Vanilla baseline, which is a Hessian-based method. W/A is the bit-width of weight and activation. * represents mixed precision (4/8 bits).

sults(76.64%, 16.5 Mb, 135.9 ms). Although OHQ is not specifically designed for QAT and is slightly lower in accuracy than current advanced methods, thanks to its on-chip awareness capabilities, the computing delay deployed on edge chips is minimized. Moreover, in MobileNetV3, the accuracy of OHQ is 0.08% and 0.46% higher than that of HAQ and GZNQ, respectively, and the compression rate of the model is 20% higher than that of GZNQ, which still shows the sota quantization performance. Notably, all the OHQ quantization models have the fastest inference on FPGA.

4.3. Ablation Results

4.3.1. HARDWARE-AWARE PARAMETERS

We present an analytical exposition of statistical insights in Fig. 5 for MobileNetV3. We unveil the sensitivities exhibited across layers(left). Notably, higher sensitivities exert a profound influence on accuracy, underscoring their pivotal role in shaping model performance. We found that the first and the last layers give higher sensitivities in each network which is since the first layer directly deals with original images or feature maps with larger aspects, while the last layer needs to perform the hidden layer classification computation that determines the output data, and is prone to accumulating errors and is sensitive to the weight changes in on-chip low-precision quantitative inference scenarios. The middle demonstrates the change of clocks, and it can be seen that the latency on-chip is not strongly correlated with the parameter number. It is more strongly correlated with the size of the input feature map of each layer, while depthwise convolution has a greater correlation between the computation time and the number of channels compared to ordinary convolution. Power consumption is predominantly shaped by parallel computation scales, indicating the reduced rate of consumption increases with large size considering power and computation efficiency. More models’ experiments are shown in Appendix A.

4.3.2. OPTIMIZATION FACTOR DECONSTRUCTION

The study conducts a comprehensive examination of compression and performance dynamics across various models. HAWQ-v3 is chosen as the foundational method, which also implements mixed-precision quantization with an awareness of hardware capabilities. The results, presented in Table 3, highlight the superior performance gains facilitated by MQE-based sensitivity. While OQA-guided hardware-aware constraints exhibit an appreciable augmentation in compression rates, the adoption of OQA as a sole optimization factor yields elevated accuracy loss in bit-width configurations. As demonstrated by Eq. 11, integrating MQE and OQA constraints produces a synergistic effect, achieving a higher compression rate while maintaining accuracy, in sharp contrast to the results obtained from using individual parameters alone. This detailed analysis highlights the complex interrelation between compression, performance, and model constraints, aiding in the making of well-informed decisions about optimization strategies and trade-offs in scenarios where resources are limited.

5. Conclusion

In this paper, our proposed OHQ introduces an innovative and effective solution for hardware-aware mixed-precision quantization, offering a substantial stride toward efficient and accurate deployment of DNNs on resource-constrained chips. Firstly, the OQA pipeline furnishes an avenue to comprehend the true efficiency metrics of quantization operators within the hardware ecosystem and yields insights that inform subsequent optimization steps. Secondly, the MQE technique is meticulously designed to efficiently gauge accuracy metrics for operators while adhering to on-chip computational constraints. Synthesizing network and hardware insights through linear programming, we derive optimal bit-width configurations. A remarkable facet of our approach is that the entire quantization process unfolds on-chip.

6. Impact Statements

This paper presents work whose goal is to advance the field of Machine Learning. There are many potential societal consequences of our work, none which we feel must be specifically highlighted here.

References

Boutros, A., Yazdanshenas, S., and Betz, V. You cannot improve what you do not measure: Fpga vs. asic efficiency gaps for convolutional neural network inference. *ACM Transactions on Reconfigurable Technology and Systems (TRETS)*, 11(3):1–23, 2018.

Cai, Y., Yao, Z., Dong, Z., Gholami, A., Mahoney, M. W., and Keutzer, K. Zeroq: A novel zero shot quantization framework. In *CVPR*, pp. 13169–13178, 2020.

Chauhan, A., Tiwari, U., et al. Post training mixed precision quantization of neural networks using first-order information. In *Proceedings of the IEEE/CVF International Conference on Computer Vision*, pp. 1343–1352, 2023.

Choi, J., Wang, Z., Venkataramani, S., Chuang, P. I.-J., Srinivasan, V., and Gopalakrishnan, K. Pact: Parameterized clipping activation for quantized neural networks. *arXiv preprint arXiv:1805.06085*, 2018.

Deng, J., Dong, W., Socher, R., Li, L.-J., Li, K., and Fei-Fei, L. Imagenet: A large-scale hierarchical image database. In *2009 IEEE conference on computer vision and pattern recognition*, pp. 248–255. Ieee, 2009.

Dong, P., Li, L., Wei, Z., Niu, X., Tian, Z., and Pan, H. Emq: Evolving training-free proxies for automated mixed precision quantization. In *Proceedings of the IEEE/CVF International Conference on Computer Vision*, pp. 17076–17086, 2023.

Dong, Z., Yao, Z., Gholami, A., Mahoney, M. W., and Keutzer, K. Hawq: Hessian aware quantization of neural networks with mixed-precision. In *Proceedings of the IEEE/CVF International Conference on Computer Vision*, pp. 293–302, 2019.

Dong, Z., Yao, Z., Arfeen, D., Gholami, A., Mahoney, M. W., and Keutzer, K. Hawq-v2: Hessian aware trace-weighted quantization of neural networks. *NeurIPS*, 33: 18518–18529, 2020.

Farooq, U. and Mehrez, H. Pre-silicon verification using multi-fpga platforms: A review. *Journal of Electronic Testing*, 37(1):7–24, 2021.

Gray, R. M. and Neuhoff, D. L. Quantization. *IEEE transactions on information theory*, 44(6):2325–2383, 1998.

Guo, K., Zeng, S., Yu, J., Wang, Y., and Yang, H. A survey of fpga-based neural network accelerator. *arXiv preprint arXiv:1712.08934*, 2017.

Han, S., Mao, H., and Dally, W. J. Deep compression: Compressing deep neural networks with pruning, trained quantization and huffman coding. *arXiv preprint arXiv:1510.00149*, 2015.

Haroush, M., Hubara, I., Hoffer, E., and Soudry, D. The knowledge within: Methods for data-free model compression. In *CVPR*, pp. 8494–8502, 2020.

He, K., Zhang, X., Ren, S., and Sun, J. Deep residual learning for image recognition. In *Proceedings of the IEEE conference on computer vision and pattern recognition*, pp. 770–778, 2016.

He, X., Lu, J., Xu, W., Hu, Q., Wang, P., and Cheng, J. Generative zero-shot network quantization. In *CVPR*, pp. 3000–3011, 2021.

Horowitz, M. 1.1 computing’s energy problem (and what we can do about it). In *2014 IEEE international solid-state circuits conference digest of technical papers (ISSCC)*, pp. 10–14. IEEE, 2014.

Howard, A., Sandler, M., Chu, G., Chen, L.-C., Chen, B., Tan, M., Wang, W., Zhu, Y., Pang, R., Vasudevan, V., et al. Searching for mobilenetv3. In *Proceedings of the IEEE/CVF international conference on computer vision*, pp. 1314–1324, 2019.

Hutton, M., Yuan, R., Schleicher, J., Baeckler, G., Cheung, S., Chua, K. K., and Phoon, H. K. A methodology for fpga to structured-asic synthesis and verification. In *Proceedings of the Design Automation & Test in Europe Conference*, volume 2, pp. 1–6. IEEE, 2006.

Krishnamoorthi, R. Quantizing deep convolutional networks for efficient inference: A whitepaper. *arXiv preprint arXiv:1806.08342*, 2018.

Li, Y., Gong, R., Tan, X., Yang, Y., Hu, P., Zhang, Q., Yu, F., Wang, W., and Gu, S. Brecq: Pushing the limit of post-training quantization by block reconstruction. *arXiv preprint arXiv:2102.05426*, 2021.

Lin, J., Rao, Y., Lu, J., and Zhou, J. Runtime neural pruning. *NeurIPS*, 30, 2017.

Ma, Y., Jin, T., Zheng, X., Wang, Y., Li, H., Wu, Y., Jiang, G., Zhang, W., and Ji, R. Ompq: Orthogonal mixed precision quantization. In *AAAI*, volume 37, pp. 9029–9037, 2023.

Markovic, D., Chang, C., Richards, B., So, H., Nikolic, B., and Brodersen, R. W. Asic design and verification in

an fpga environment. In *2007 IEEE Custom Integrated Circuits Conference*, pp. 737–740. IEEE, 2007.

Nagel, M., Baalen, M. v., Blankevoort, T., and Welling, M. Data-free quantization through weight equalization and bias correction. In *Proceedings of the IEEE/CVF International Conference on Computer Vision*, pp. 1325–1334, 2019.

Nurvitadhi, E., Sim, J., Sheffield, D., Mishra, A., Krishnan, S., and Marr, D. Accelerating recurrent neural networks in analytics servers: Comparison of fpga, cpu, gpu, and asic. In *2016 26th International Conference on Field Programmable Logic and Applications (FPL)*, pp. 1–4. IEEE, 2016.

Park, E. and Yoo, S. Profit: A novel training method for sub-4-bit mobilenet models. In *Computer Vision–ECCV 2020: 16th European Conference, Glasgow, UK, August 23–28, 2020, Proceedings, Part VI 16*, pp. 430–446. Springer, 2020.

Qin, H., Ding, Y., Zhang, X., Wang, J., Liu, X., and Lu, J. Diverse sample generation: Pushing the limit of generative data-free quantization. *IEEE Transactions on Pattern Analysis and Machine Intelligence*, 2023.

Shawahna, A., Sait, S. M., and El-Maleh, A. Fpga-based accelerators of deep learning networks for learning and classification: A review. *ieee Access*, 7:7823–7859, 2018.

Shen, S., Dong, Z., Ye, J., Ma, L., Yao, Z., Gholami, A., Mahoney, M. W., and Keutzer, K. Q-bert: Hessian based ultra low precision quantization of bert. In *AAAI*, volume 34, pp. 8815–8821, 2020.

Wang, K., Liu, Z., Lin, Y., Lin, J., and Han, S. Haq: Hardware-aware automated quantization with mixed precision. In *CVPR*, pp. 8612–8620, 2019.

Wu, B., Wang, Y., Zhang, P., Tian, Y., Vajda, P., and Keutzer, K. Mixed precision quantization of convnets via differentiable neural architecture search. *arXiv preprint arXiv:1812.00090*, 2018.

Yang, C.-T., Wang, H.-Y., Ou, W.-S., Liu, Y.-T., and Hsu, C.-H. On implementation of gpu virtualization using pci pass-through. In *4th IEEE International Conference on Cloud Computing Technology and Science Proceedings*, pp. 711–716. IEEE, 2012.

Yang, L. and Jin, Q. Fracbits: Mixed precision quantization via fractional bit-widths. In *AAAI*, volume 35, pp. 10612–10620, 2021.

Yao, Z., Dong, Z., Zheng, Z., Gholami, A., Yu, J., Tan, E., Wang, L., Huang, Q., Wang, Y., Mahoney, M., et al. Hawq-v3: Dyadic neural network quantization. In *ICML*, pp. 11875–11886. PMLR, 2021.

Zhao, R., Hu, Y., Dotzel, J., De Sa, C., and Zhang, Z. Improving neural network quantization without retraining using outlier channel splitting. In *ICML*, pp. 7543–7552. PMLR, 2019.

Zhou, Y., Moosavi-Dezfooli, S.-M., Cheung, N.-M., and Frossard, P. Adaptive quantization for deep neural network. In *AAAI*, volume 32, 2018.

Zhu, C., Han, S., Mao, H., and Dally, W. J. Trained ternary quantization. *arXiv preprint arXiv:1612.01064*, 2016.

A. On-chip Comparison

Fig. 6 further shows on-chip awareness characteristics of ResNet-18, MobileNet-v2 and MobileNet-v3. It further proves that the computing clock cycle and power consumption of the hardware cannot simply correspond to the amount of model parameters. However, OHQ obtains on-chip attributes of the neural networks more accurately through hardware perception.

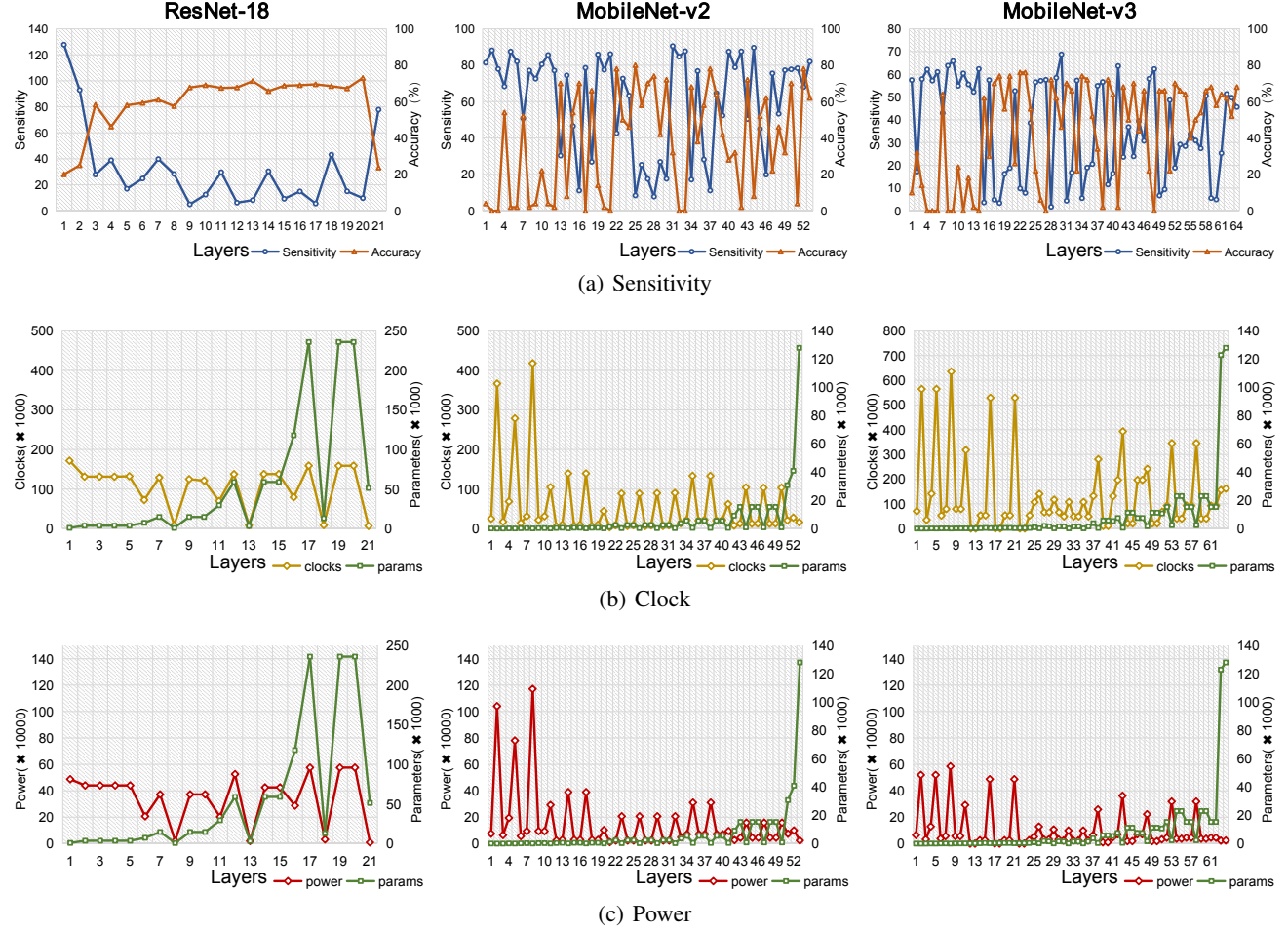


Figure 6. Comparison of on-chip perceptual parameters with the characteristics of the models. ResNet18, MobileNetV2, and MobileNetV3 are selected (from left to right), and the sensitivities from MQE and the clock information obtained from OQA, as well as the power consumption estimates, are obtained through the OHQ.

B. Hardware Implementation Details

B.1. Img2Col

Much of the literature shows that the primitive way of computing convolution requires frequent jumps to access the data, which is a cache-unfriendly way of accessing the data, and therefore, it is difficult to fully exploit the processor power by computing the convolution directly by definition. Img2Col is a method of reordering the raw data of a convolution operator to make it suitable for computation. Demonstrated in the left part of Fig. 7, this method converts the convolution operation into a matrix multiplication operation, thus concentrating the originally dispersed convolution kernel into a local region, which can increase the probability of local access during computation, and at the same time, it also reduces a kind of operation that should be designed for complex computation mechanism to the same computation as the fully connected one, which unifies the computation method, reduces the cost of design, and facilitates the unification of perception of its operation cycle and performance.

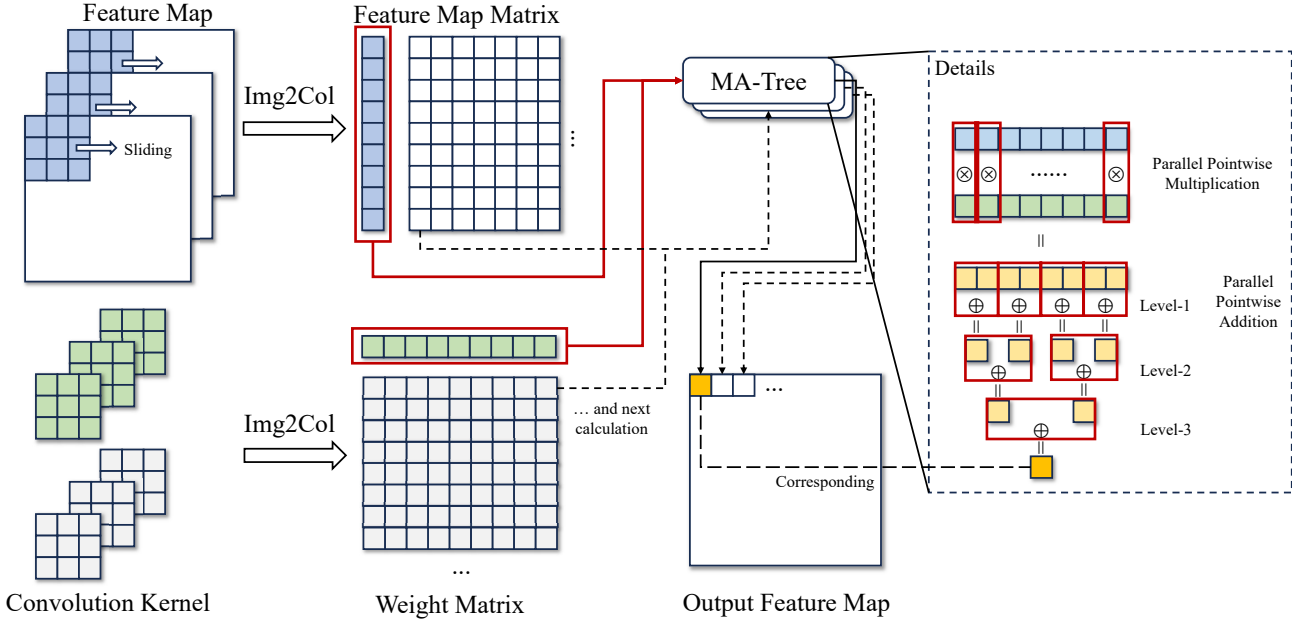


Figure 7. This is an overall illustration of Img2Col and Multiplication-Add Tree. The Img2Col method converts convolutional computation into matrix multiplication by rearranging the data in the feature map and convolution kernel. Then, these matrices will be fed into arrays consisting of Multiplication-Addition Trees. After a step-by-step and level-by-level calculation, we obtain elements of the result and combine them into an output matrix.

To perform the calculation, Img2Col first expands the convolution kernel and feature map into matrices and multiplies them together to produce the output, with the convolution kernel matrix on the left and the feature map matrix on the right. For the convolution kernel, each of its output channels is treated as a row of the convolution kernel matrix, and the data in that output channel is filled into that row in the order in which it was computed. This results in a convolution kernel matrix of size $(k_o) \times (k_i, k_h, k_w)$. For the feature map, the data multiplied each time by the convolution kernel counterpart is arranged in order as a column of the feature map matrix, with different columns for the data at different locations covered multiple times by the convolution kernel. This gives the size of the feature map matrix as $(in_c, k_h, k_w) \times (out_h, out_w)$, under known condition $k_i = in_c$. Multiplying the two gives the output matrix with dimensions $(k_o) \times (out_h, out_w)$, whose data is arranged in the same order as the input feature maps and can be used to compute the next layer of operators in the neural network without extra rearranging.

On the whole, this rearrangement method is mainly performed from two perspectives: for the input feature map, it flattens and splices the data of different channels at the same sliding window position; for the convolution kernel, it treats different channels in the same convolution kernel in the same way and finally obtains the matrix obtained by splicing the columns from the window transformations. In this way, the data scattered in space becomes continuous during computation, making it easy to hit the cache and convenient for FPGA transfer and computation logic.

B.2. Multiplication-Addition Tree

Since we have converted the convolution operation into a matrix operation in Img2Col, as shown in the right part of Fig. 7, we can use only one computational mechanism to complete the matrix multiplication operation. Here, we use the Multiplication-Addition Tree to complete the matrix operation, whose operation mechanism regards vector dot product as the basic calculation step. Each time the calculation of the input is a pair of two vectors of the same length, that is, the matrix operation of the two input matrices in the selection of columns or rows of data. The multiplication tree will group the elements at the corresponding positions of the two inputs into two-by-two groups in a front-to-back order, and then multiply each group internally to get the result of the group. After the point multiplication is the continuous addition with the accumulation of the intermediate results, where there is no dependence on each other, so we can continue to divide and

Algorithm 1 Split Matrix

Input: Length of the side of each weight or each feature map matrix $\{L_1, L_2, \dots, L_n\}$

Output: The tile side length $\{T_1, T_2, \dots, T_n\}$ of each layer

```

1:  $L_{\max} \leftarrow \max\{L_1, L_2, \dots, L_n\}$ 
2:  $L_{\min} \leftarrow \min\{L_1, L_2, \dots, L_n\}$ 
3: for  $i = 1, 2, \dots, n$  do
4:   if  $L_i \leq L_{\max}$  then
5:     if  $L_i$  is power of 2 then
6:        $T_i \leftarrow L_{\max}$ 
7:     else
8:       if  $L_i < L_{\min}$  then
9:          $T_i \leftarrow L_{\min}$ 
10:      else
11:         $n \leftarrow \text{floor}(\log_2 L_i)$ 
12:        if  $L_i > \frac{2^n + 2^{n+1}}{2}$  then
13:           $T_i \leftarrow 2^{n+1}$ 
14:        else
15:           $T_i \leftarrow 2^n$ 
16:        end if
17:      end if
18:    end if
19:  else
20:     $n \leftarrow L_i \bmod L_{\max}$ 
21:    if  $n > \frac{L_{\max}}{2}$  then
22:       $T_i \leftarrow L_{\max}$ 
23:    else
24:       $T_i \leftarrow \frac{L_{\max}}{2}$ 
25:    end if
26:  end if
27: end for
28: return  $\{T_1, T_2, \dots, T_i\}$ 

```

calculate them in parallel with each other, forming a binary tree. Besides being able to parallelize the elements of the same step of the operation, such a computational mechanism can also be employed to add the appropriate flow processing logic, so that manage the data stream continuously.

B.3. Sub Matrix Slicing

We have already looked at how to convert and compute convolutions and other matrix multiplication operations, now we look at optimizing matrix multiplication. Consider a matrix multiplication between two matrices of side length L , whose sliced blocks are of side length M . Let L be an integer multiple N of M . Each matrix can be sliced into N^2 sub-matrix blocks of side length M and requires N^3 sub-matrix multiplications and the corresponding accumulations to obtain the final result. In these N^3 sub-matrix multiplications, two input matrices of size M^2 and one result matrix must be transmitted each time, i.e. the total amount of data to be transmitted is:

$$C = 3M^2N^3 = \frac{3L^3}{M} \quad (13)$$

It can be seen that the total amount of data transferred C decreases monotonically with the side length M of the sliced submatrix block. In FPGA acceleration of neural networks, there is a trade-off between reducing the total amount of data transferred and reducing inefficient computation. On the one hand, on-chip and off-chip data transfer is often a performance bottleneck, so the total amount of data transferred must be minimized, as shown in Equation 13, and the size of the sliced submatrix block must be increased. On the other hand, since the matrix may need to be extended to align the data during slicing to accommodate the design logic of the FPGA if the original matrix edge length is not a power of 2, this may lead to an increase in the amount of data to be transferred, especially the invalid data, so the length of the extension must be reduced and the block size of the sliced sub-matrix urgently reduced. In addition, to facilitate the computation of small matrices, it is necessary to restrict the individual matrices to be able to fill at least one row of the input buffer, i.e. the minimum side length of the matrix $L_{\min} \geq \sqrt{L_{\max}}$ must be satisfied. According to the above principle, the original matrix is chunked: the smallest of the 4 edges of the original matrix is taken as the edge length to be sliced. If the matrix edge length is a power of 2 and does not exceed L_{\max} , then this edge length is taken directly as the slicing length; otherwise, if the matrix edge length is less than L_{\min} , then L_{\min} is taken as the slicing length; otherwise if it is less than 64, it is extended to the next power of 2. If the matrix edge length is greater than L_{\max} , then L_{\max} is taken as the slicing length; otherwise, it is extended to the next power of 2; otherwise extend it to the next power of 2; if the matrix edge length is greater than L_{\max} , then take the remainder

Algorithm 2 BRAM Analyses

Input: BRAM limits B_{\max}
Output: BRAM allocation for weight, feature map, and output buffer B_w, B_f, B_o and the side length L_{\max} of the maximum matrix to be multiplied.

```

1: let  $L_{\max}$  be a power of 2, for example  $L_{\max} \leftarrow 8$ 
2: while true do
3:    $B_w \leftarrow L_{\max} \times \text{BRAM\_coe\_for\_weight}$            {Depend on the organization of BRAM for weight storage}
4:    $B_f \leftarrow L_{\max} \times \text{BRAM\_coe\_for\_feature\_map}$    {Depend on the organization of BRAM for feature map storage}
5:    $B_o \leftarrow L_{\max} \times \text{BRAM\_coe\_for\_output}$           {Depend on the organization of BRAM for output storage}
6:   if  $B_w + B_f + B_o \leq B_{\max}$  then
7:      $L_{\max} \leftarrow 2 \times L_{\max}$ 
8:   else
9:     break
10:  end if
11: end while
12:  $L_{\max} \leftarrow \frac{L_{\max}}{2}$ 
13:  $B_w \leftarrow L_{\max} \times \text{BRAM\_coe\_for\_weight}$ 
14:  $B_f \leftarrow L_{\max} \times \text{BRAM\_coe\_for\_feature\_map}$ 
15:  $B_o \leftarrow L_{\max} \times \text{BRAM\_coe\_for\_output}$ 
16: return  $B_w, B_f, B_o, L_{\max}$ 
    
```

of the matrix edge length at L_{\max} . If the remainder is greater than $L_{\max}/2$, then make the slicing length L_{\max} , otherwise make the slicing length $L_{\max}/2$. Using the matrix slicing Algorithm 1, the original matrix can be sliced into appropriate sizes so that the size of each of these matrices does not exceed the capacity of the on-chip memory.

B.4. BRAM Merges and Allocation

Finally, we need to consider the details of implementing matrix multiplication on a particular model of FPGA. The most important of these is the organization of the data. The ZYNQ platform provides a BRAM structure, which is more suitable for generating memory units for centralized processing than distributed RAM generated using LUTs. Normally BRAM is 72 bits wide, and we use only 64 bits of this as an 8-byte unit to facilitate the alignment process and simplify the logic. Obviously, this width is not enough to handle a large number of large bit-width data, so we usually splice it to get a large bit-width memory space, which is convenient for data transfer, caching and positioning; at the same time, we also need to pay attention to the limit of the amount of BRAM, which cannot exceed the limit that the FPGA can provide, so we use the following Algorithm 2 to limit the amount of BRAM usage as a simple segmentation example. The idea here is to allocate BRAM by controlling the input to limit space one column at a time, and the output is cached on the chip as much as possible for accumulation, so the output consumes more BRAM relatively to reduce repeated transmission.